

Cite this: *Mater. Adv.*, 2025,  
6, 3139Received 15th January 2025,  
Accepted 31st March 2025

DOI: 10.1039/d5ma00037h

rsc.li/materials-advances

# Vertical p-GaN/n-Ga<sub>2</sub>O<sub>3</sub> heterojunction diode with high switching performance

Phuc Hong Than,<sup>a</sup> Tho Quang Than<sup>b</sup> and Yasushi Takaki<sup>c</sup>

Although the forward current–voltage characteristics and breakdown voltage performance of GaN/Ga<sub>2</sub>O<sub>3</sub> p–n diodes have been extensively studied, there have been no reports on their reverse recovery characteristics. This paper investigates the reverse recovery behavior of p-GaN/n-Ga<sub>2</sub>O<sub>3</sub> diodes and examines the effects of temperature, forward current magnitude, and doping concentration on their performance. In the simulations of the switching process, a reverse voltage ( $V_R$ ) of  $-10$  V and a forward current ( $I_F$ ) of 3 A were applied. The p-GaN/n-Ga<sub>2</sub>O<sub>3</sub> diode demonstrated fast reverse recovery, achieving a reverse recovery time ( $t_{rr}$ ) of 72 ns, outperforming 6H-SiC p–n diodes under identical  $dI/dt$  conditions. Notably, the reverse recovery characteristics of the p-GaN/n-Ga<sub>2</sub>O<sub>3</sub> diode remained stable across varying temperatures and forward current levels. Additionally, a high breakdown voltage of 703 V was achieved at 300 K, maintaining stability across different temperatures. These findings highlight the potential of p-GaN/n-Ga<sub>2</sub>O<sub>3</sub> heterojunction diodes for high-voltage, fast-switching applications.

## 1. Introduction

In recent years, beta-gallium oxide ( $\beta$ -Ga<sub>2</sub>O<sub>3</sub>) has gained significant attention as a promising candidate for next-generation power electronic applications due to its wide-bandgap semiconductor properties. With a bandgap of approximately 4.7–4.9 eV, a high critical electric field of around 8 MV cm<sup>-1</sup>, and an exceptional Baliga's figure of merit (BFOM),  $\beta$ -Ga<sub>2</sub>O<sub>3</sub> exhibits superior characteristics compared to conventional materials such as silicon (Si) and has an expected electric field that is several times higher than that of silicon carbide (SiC) and gallium nitride (GaN).<sup>1–7</sup> Additionally,  $\beta$ -Ga<sub>2</sub>O<sub>3</sub> offers the advantage of cost-effective, large-scale production, made possible by the availability of large, defect-reduced wafers manufactured using techniques such as edge-defined film-fed growth (EFG).<sup>8</sup>

However, one of the main challenges facing Ga<sub>2</sub>O<sub>3</sub> is the lack of p-type doping. As a result, research on Ga<sub>2</sub>O<sub>3</sub>-based devices has primarily focused on high-electron-mobility transistors (HEMTs), Schottky barrier diodes (SBDs), and metal-oxide–semiconductor field-effect transistors (MOSFETs).<sup>9–22</sup> To overcome this limitation, alternative materials such as NiO, Cu<sub>2</sub>O, and GaN have been investigated as potential substitutes

for p-type Ga<sub>2</sub>O<sub>3</sub>.<sup>23–27</sup> Among these, GaN/ $\beta$ -Ga<sub>2</sub>O<sub>3</sub> p–n heterojunctions have shown promising rectifying behavior and improved breakdown voltages when created through mechanical exfoliation.<sup>28,29</sup> GaN, in particular, stands out due to its wide bandgap and its ability to be epitaxially grown on  $\beta$ -Ga<sub>2</sub>O<sub>3</sub> using metal–organic chemical vapor deposition (MOCVD), taking advantage of their well-defined crystallographic alignment.<sup>30–32</sup>

The reverse recovery characteristics of power diodes have been extensively studied in other representative wide-bandgap semiconductors, but the reverse recovery behavior of GaN/ $\beta$ -Ga<sub>2</sub>O<sub>3</sub> heterojunction p–n diodes has not been explored. This is particularly significant because the combination of GaN and  $\beta$ -Ga<sub>2</sub>O<sub>3</sub> introduces unique physical mechanisms due to their distinct material properties and interface characteristics. These mechanisms could greatly impact the reverse recovery characteristics, yet this aspect has not been thoroughly investigated in the literature. In this study, we examine the reverse recovery characteristics of GaN/ $\beta$ -Ga<sub>2</sub>O<sub>3</sub> heterojunction diodes, specifically focusing on the effects of temperature, forward current magnitude and doping concentration. This research provides a novel contribution to understanding the reverse recovery dynamics in ultra-wide bandgap semiconductor devices.

## 2. Structure and mechanism

### 2.1. Device structure

Fig. 1 depicts a schematic representation of a simulated GaN/ $\beta$ -Ga<sub>2</sub>O<sub>3</sub> heterojunction p–n diode. This study focuses on simulating the diode and evaluating the reliability of its reverse

<sup>a</sup> Duy Tan University (DTU), 3 Quang Trung, Hai Chau Dist., Danang 550000, Vietnam. E-mail: thanhongphuc@duytan.edu.vn

<sup>b</sup> Central Power Corporation (EVNCP), 78A Duy Tan, Hoa Thuan Dong, Hai Chau, Danang 550000, Vietnam

<sup>c</sup> Power Device Works, Mitsubishi Electric Corporation, 997, Miyoshi, Koushi-Shi, Kumamoto 861-1197, Japan



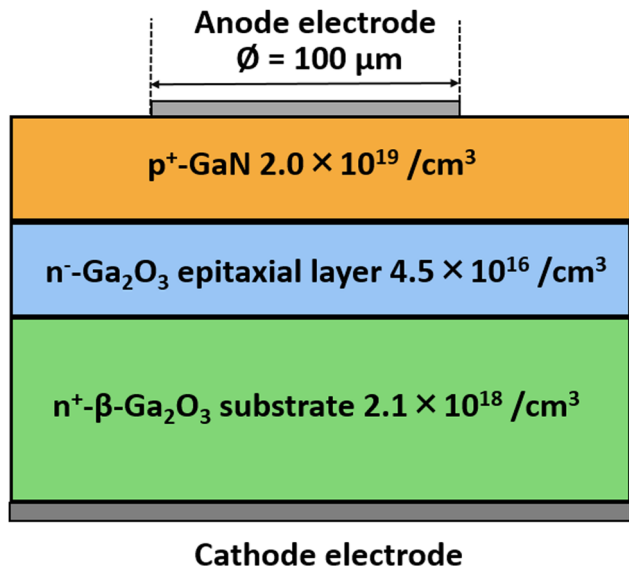


Fig. 1 Schematic representation of the simulated GaN/ $\beta$ -Ga<sub>2</sub>O<sub>3</sub> hetero-junction p-n diode.

recovery characteristics using technology computer-aided design (TCAD) tools. The n-Ga<sub>2</sub>O<sub>3</sub> epitaxial layer has a thickness of 3.8  $\mu$ m and a doping concentration of  $4.5 \times 10^{16} \text{ cm}^{-3}$ , while the n-Ga<sub>2</sub>O<sub>3</sub> substrate has a thickness of 8.0  $\mu$ m and a doping concentration of  $2.1 \times 10^{18} \text{ cm}^{-3}$ .<sup>29,31</sup> The p-GaN layer has a thickness of 3.2  $\mu$ m and a doping concentration of  $2.0 \times 10^{19} \text{ cm}^{-3}$ . The material properties of  $\beta$ -Ga<sub>2</sub>O<sub>3</sub> and GaN, such as bandgap, electron mobility, electron affinity, dielectric constant, and thermal conductivity, were obtained from previous research<sup>2,21,22,32–34,35–40</sup> and are summarized in Tables 1 and 2, respectively. To calibrate the simulation model, experimental results from  $\beta$ -Ga<sub>2</sub>O<sub>3</sub> Schottky barrier diode (SBD)<sup>25</sup> and GaN p-n diode<sup>41</sup> were utilized. The simulated  $I$ - $V$  characteristics closely match the reported experimental data, as shown in Fig. 2(a) for the Ga<sub>2</sub>O<sub>3</sub> SBD and Fig. 2(b) for the GaN p-n diode.

## 2.2. Models and parameters used in simulations

The performance of the device was evaluated using 2D device simulators that solve Poisson's equation, along with the continuity and

drift-diffusion equations.<sup>42–48</sup> These simulations, which also included mixed-mode analyses, were conducted using TCAD tools. During the forward turn-on phase, the p-n junction is positively biased, allowing for carrier conduction. When the device transitions to the off state, the transverse electric field drives the non-equilibrium carriers within the device back to equilibrium. The simulation of the GaN/ $\beta$ -Ga<sub>2</sub>O<sub>3</sub> hetero-junction p-n diode incorporates key physical models such as Shockley-Read-Hall and Auger recombination to account for carrier recombination mechanisms, concentration-dependent mobility, and lateral electric field-dependent mobility to capture variations in carrier transport behavior. Additionally, bandgap narrowing is included to model changes in the energy band structure under specific conditions.

(1) Carrier generation-recombination models: the numerical simulation of carrier generation and recombination is carried out using concentration-dependent models for Shockley-Read-Hall (SRH) and Auger recombination.<sup>46–48</sup>

$$R_{\text{SRH}} = \frac{pn - n_i^2}{\tau_{p0} \left[ n + n_i \exp\left(\frac{E_t - E_i}{kT}\right) \right] + \tau_{n0} \left[ p + n_i \exp\left(\frac{-E_t - E_i}{kT}\right) \right]} \quad (1)$$

$$R_{\text{Auger}} = 3 \times 10^{-29}(pn^2 - nn_i^2) + 3 \times 10^{-29}(np^2 - pn_i^2) \quad (2)$$

Here,  $n_i$  represents the effective intrinsic carrier concentration,  $E_t$  denotes the recombination center energy level,  $E_i$  is the intrinsic Fermi level, and  $\tau_{n0}$  and  $\tau_{p0}$  represent the electron and hole lifetimes, respectively.

(2) Impact ionization model: the equation describes the rate of carrier generation during the avalanche breakdown process.<sup>49</sup>

$$G = \alpha_n J_n + \alpha_p J_p \quad (3)$$

Here,  $\alpha_n$  and  $\alpha_p$  represent the impact ionization coefficients for electrons and holes, respectively, while  $J_n$  and  $J_p$  denote the electron and hole current densities. The ionization rate is effectively

Table 1 Fundamental material properties of  $\beta$ -Ga<sub>2</sub>O<sub>3</sub> used in the simulation

Parameter	Value
Bandgap (eV)	4.8 (ref. 21)
Conduction band offset (eV)	0.165 (ref. 32)
Valence band offset (eV)	1.625 (ref. 32)
Electron mobility ( $\text{cm}^2 \text{ V}^{-1} \text{ s}^{-1}$ )	118 (ref. 22)
Hole mobility ( $\text{cm}^2 \text{ V}^{-1} \text{ s}^{-1}$ )	10 (ref. 22)
Thermal conductivity ( $\text{W cm}^{-1} \text{ K}^{-1}$ )	0.13 (ref. 2)
Dielectric constant	10.2 (ref. 33)
Electron affinity (eV)	4.0 (ref. 21)
Effective density of states in the conduction band/valence band ( $\text{cm}^{-3}$ )	$3.72 \times 10^{18}$ (ref. 21)
Effective density of states in the valence band ( $\text{cm}^{-3}$ )	$1.16 \times 10^{19}$ (ref. 21)
Impact ionization coefficients $a_n$ ( $\text{cm}^{-1}$ )	$0.79 \times 10^6$ (ref. 34)
Impact ionization coefficients $b_n$ ( $\text{V cm}^{-1}$ )	$2.92 \times 10^6$ (ref. 34)
Electron lifetime (s)	$2.0 \times 10^{-10}$ (ref. 22)
Hole lifetime (s)	$2.1 \times 10^{-8}$ (ref. 22)



Table 2 Fundamental material properties of GaN used in the simulation

Parameter	Value
Bandgap (eV)	3.53 (ref. 35)
Dielectric constant	8.9 (ref. 36)
Electron affinity (eV)	4.1 (ref. 37)
Effective density of states in the conduction band (cm <sup>-3</sup> )	2.3 × 10 <sup>18</sup> (ref. 38)
Effective density of states in the valence band (cm <sup>-3</sup> )	3.5 × 10 <sup>19</sup> (ref. 38)
Impact ionization coefficients $a_n$ (cm <sup>-1</sup> )	1.56 × 10 <sup>5</sup> (ref. 39)
Impact ionization coefficients $b_n$ (V cm <sup>-1</sup> )	1.41 × 10 <sup>7</sup> (ref. 39)
Electron lifetime (s)	1.0 × 10 <sup>-9</sup> (ref. 40)
Hole lifetime (s)	1.0 × 10 <sup>-9</sup> (ref. 40)

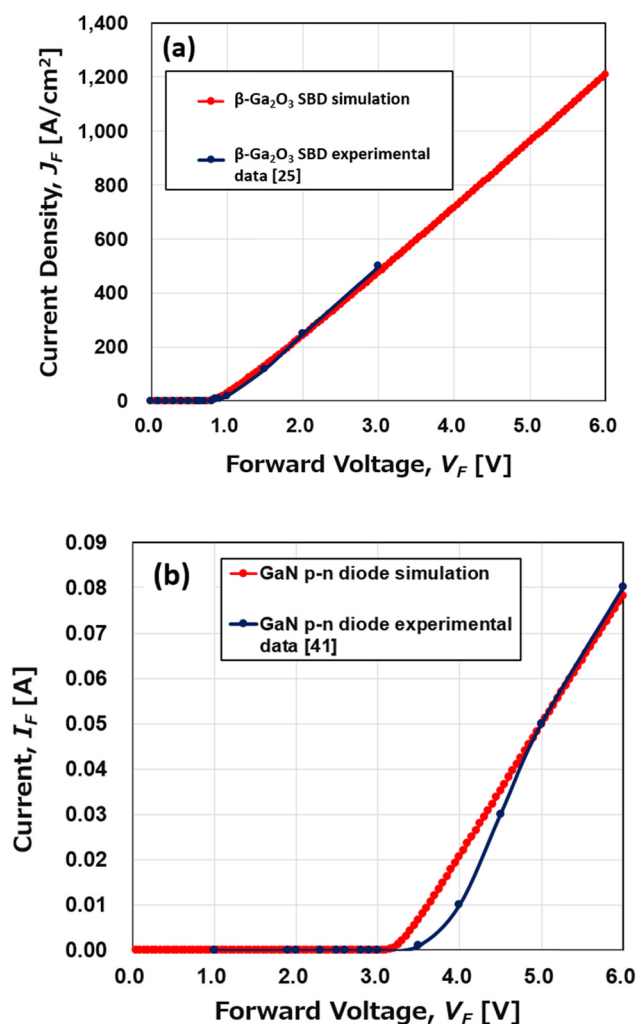


Fig. 2 Experimental data (blue) and simulated data (red) for the forward current–voltage ( $I$ – $V$ ) characteristics of (a)  $\beta$ -Ga<sub>2</sub>O<sub>3</sub> SBD and (b) GaN p–n diode. Good agreement confirms the accuracy of the DC device model.

modeled using the Selberherr model.

$$\alpha_{n,p} = A_{n,p} \exp \left[ \left( \frac{B_{n,p}}{E} \right)^{C_{n,p}} \right] \quad (4)$$

Here,  $E$  represents the electric field along the direction of current flow, and  $A_{n,p}$ ,  $B_{n,p}$ , and  $C_{n,p}$  are the respective fitting coefficients.

(3) Thermal conductivity specification: we performed 2D physics-based electrothermal device simulations through TCAD.<sup>50</sup> These simulations involved solving coupled drift-diffusion and heat flow equations.

### 3. Results and discussion

We used TCAD to simulate the band diagram of the heterojunction, as shown in Fig. 3. By selecting the appropriate electron affinity values for GaN and Ga<sub>2</sub>O<sub>3</sub>, we obtained a conduction band offset ( $\Delta E_c$ ) of 0.165 eV and a valence band offset ( $\Delta E_v$ ) of 1.625 eV. These values were chosen to match the required band offsets, in accordance with experimental data. The resulting band offset values are consistent with those reported by W. Li *et al.*<sup>32</sup> using X-ray photoelectron spectroscopy.

The simulated forward current–voltage ( $I$ – $V$ ) characteristics of the GaN/ $\beta$ -Ga<sub>2</sub>O<sub>3</sub> p–n diode at 300 K are illustrated in Fig. 4. When a forward bias is applied, the diode exhibits rectifying behavior, and the turn-on voltage is the point at which the current begins to increase. The turn-on voltage ( $V_{on}$ ) is observed to be 3.5 V, which is in reasonable agreement with experimental results.<sup>28</sup>

Fig. 5 illustrates the simulated temperature-dependent forward current–voltage characteristics of the GaN/ $\beta$ -Ga<sub>2</sub>O<sub>3</sub> p–n diode. It can be observed that the turn-on voltage ( $V_{on}$ )

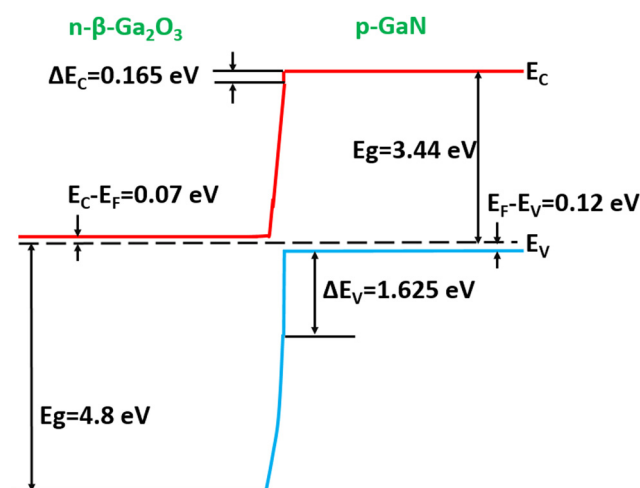


Fig. 3 Simulated band diagram of the p-GaN/ $\beta$ -Ga<sub>2</sub>O<sub>3</sub> heterojunction.



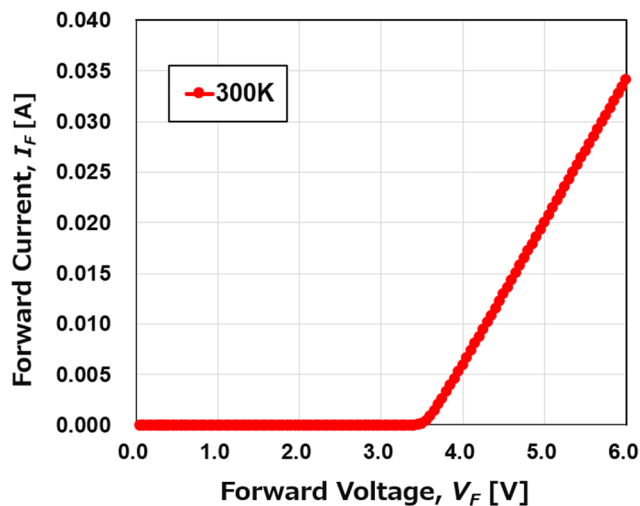


Fig. 4 Simulated forward current–voltage ( $I$ – $V$ ) characteristics of the GaN/ $\beta$ -Ga<sub>2</sub>O<sub>3</sub> p–n diode at 300 K.

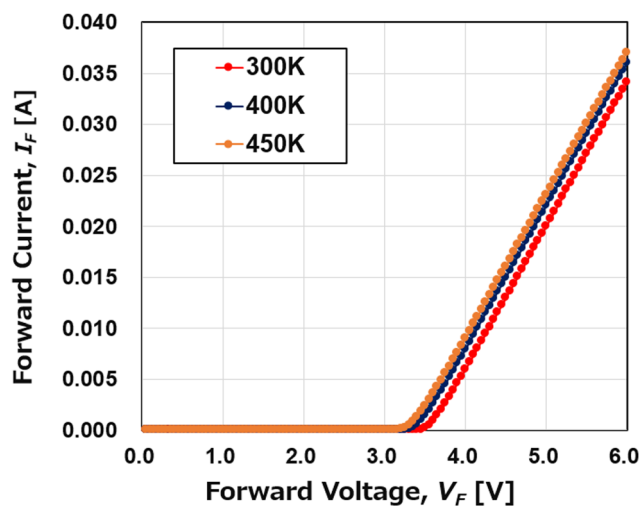


Fig. 5 Simulated temperature-dependent forward current–voltage ( $I$ – $V$ ) characteristics of the GaN/ $\beta$ -Ga<sub>2</sub>O<sub>3</sub> p–n diode.

decreases from 3.5 V to 3.25 V, and the specific on-resistance ( $R_{\text{on,sp}}$ ) in the current range from 0.02 A to 0.03 A decreases from 5.9 m $\Omega$  cm<sup>2</sup> to 5.5 m $\Omega$  cm<sup>2</sup> as the temperature rises from 300 K to 450 K. The decrease in turn-on voltage can be attributed to the increase in diffusion current across the p–n heterojunction and the bandgap narrowing effect at higher temperatures. Similarly, the decrease in  $R_{\text{on,sp}}$  with increasing temperature can be explained by the thermally enhanced conductivity modulation effect. As the temperature rises, the injection of minority carriers (holes) from p-GaN into n- $\beta$ -Ga<sub>2</sub>O<sub>3</sub> increases, leading to a decrease in space-charge resistance in the drift region. Additionally, the thermal generation of electron–hole pairs increases at higher temperatures, improving the conductivity of the drift region and resulting in more efficient current conduction.

Fig. 6 illustrates the simulated temperature-dependent reverse breakdown characteristics of the GaN/ $\beta$ -Ga<sub>2</sub>O<sub>3</sub>

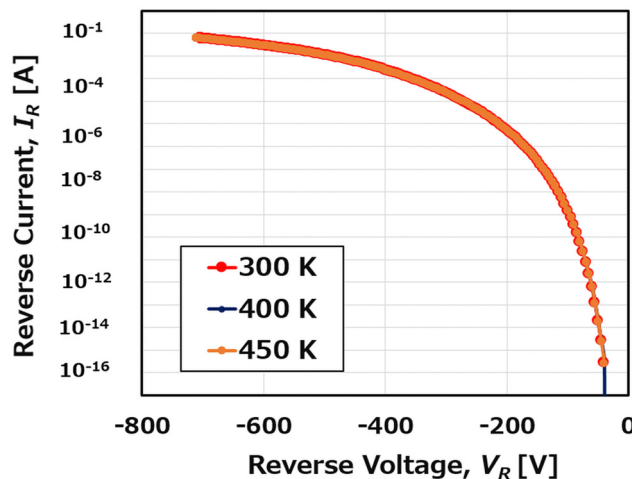


Fig. 6 Simulated temperature-dependent reverse breakdown characteristics of the GaN/ $\beta$ -Ga<sub>2</sub>O<sub>3</sub> p–n diode.

heterojunction p–n diode. It is found that the breakdown voltage remains consistent at 703 V across various temperatures, indicating the excellent temperature stability of the diode. The sharp increase in reverse current near the breakdown voltage suggests that the breakdown is dominated by avalanche breakdown. This occurs when high-energy carriers generate additional charge carriers through impact ionization, resulting in an accelerated current flow. Furthermore, Y. Duan *et al.* reported that the measured breakdown voltage increases with rising temperature, indicating that the diode with a triple-zone junction termination extension structure achieves avalanche-limited breakdown.<sup>51</sup> These findings demonstrate the excellent temperature stability of the p-GaN/n- $\beta$ -Ga<sub>2</sub>O<sub>3</sub> diode and confirm its ability to achieve avalanche-limited breakdown. In addition, Fig. 7 displays the electric field distribution at breakdown for the GaN/ $\beta$ -Ga<sub>2</sub>O<sub>3</sub> p–n diode. The analysis clearly reveals a significant concentration of the electric field at the p-GaN and n-Ga<sub>2</sub>O<sub>3</sub> junction, which can lead to catastrophic damage at this location. These results suggest that using  $\beta$ -Ga<sub>2</sub>O<sub>3</sub> material in heterojunction p–n diodes has the potential to achieve high breakdown voltages by minimizing electric field concentration and leakage current. This highlights the potential application of the p-GaN/n-Ga<sub>2</sub>O<sub>3</sub> heterojunction diode as a power device for high-voltage operations.

The reverse recovery characteristics of the GaN/ $\beta$ -Ga<sub>2</sub>O<sub>3</sub> p–n diode were investigated and compared to those of the 6H-SiC p–n diode under the same  $dI/dt$  conditions. Fig. 8 illustrates the cross-sectional schematic of the 6H-SiC p–n diode used for comparison with the GaN/ $\beta$ -Ga<sub>2</sub>O<sub>3</sub> p–n diode.<sup>52</sup> The 6H-SiC p–n diode consists of a 3.8- $\mu$ m-thick n-type epitaxial layer on an 8- $\mu$ m-thick n<sup>+</sup>-type 6H-SiC substrate with a doping concentration of approximately  $2.1 \times 10^{18}$  cm<sup>-3</sup>. The n-type epitaxial layer has a doping concentration of about  $4.5 \times 10^{16}$  cm<sup>-3</sup>. The device also includes a 3.2- $\mu$ m-thick p<sup>+</sup>-type 6H-SiC layer with a doping concentration of approximately  $2.0 \times 10^{19}$  cm<sup>-3</sup>. The material parameters for 6H-SiC are provided in Table 3.<sup>53</sup> For simulating the reverse recovery characteristics, the parameters



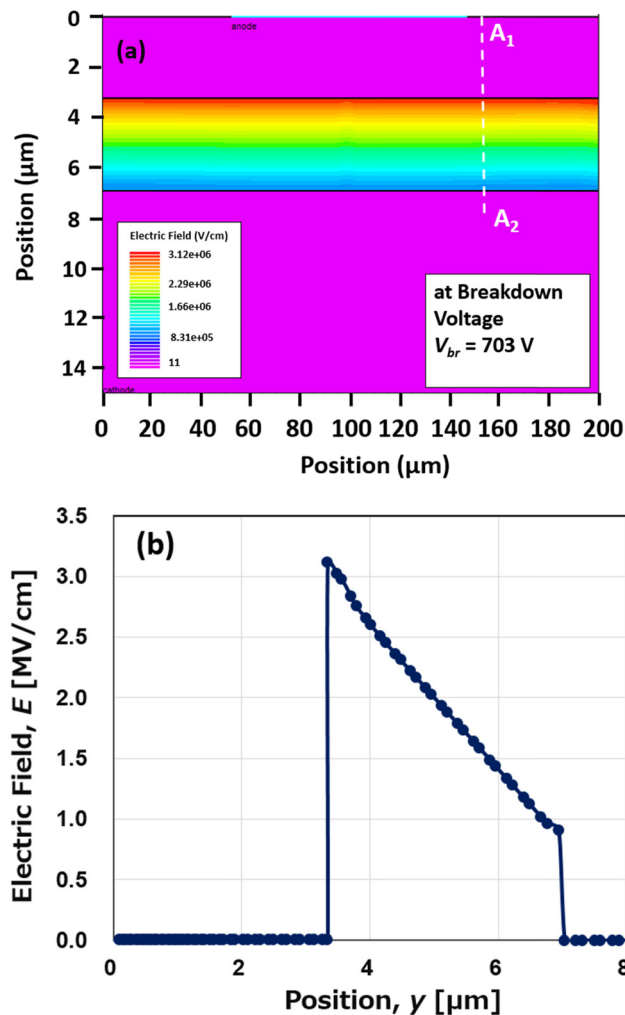


Fig. 7 Simulated electric field distributions of the GaN/ $\beta$ -Ga<sub>2</sub>O<sub>3</sub> p-n diode at breakdown: (a) two-dimensional distribution of the electric field; (b) line profile of the electric field along A<sub>1</sub>-A<sub>2</sub>.

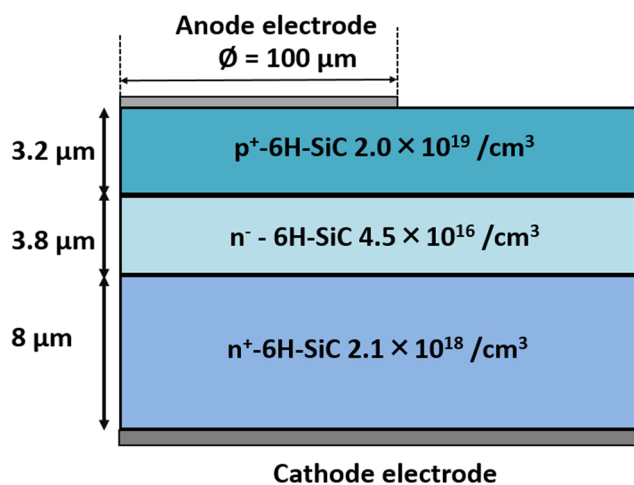


Fig. 8 Schematic representation of the simulated 6H-SiC p-n diode.<sup>52</sup>

Table 3 Fundamental material properties of 6H-SiC used in the simulation<sup>53</sup>

Parameter	Value
Bandgap (eV)	2.9
Electron lifetime (s)	$1.0 \times 10^{-9}$
Hole lifetime (s)	$1.0 \times 10^{-9}$
Electron mobility ( $\text{cm}^2 \text{V}^{-1} \text{s}^{-1}$ )	330
Thermal conductivity ( $\text{W cm}^{-1} \text{K}^{-1}$ )	5.0
Dielectric constant	9.66
Electron saturation velocity ( $\text{cm s}^{-1}$ )	$2.0 \times 10^7$
Effective density of states in the conduction band ( $\text{cm}^{-3}$ )	$7.68 \times 10^{18}$
Effective density of states in the valence band ( $\text{cm}^{-3}$ )	$4.76 \times 10^{18}$

for the diode components were set as follows: a reverse voltage ( $V_R$ ) of  $-10$  V and a forward current ( $I_F$ ) of 3 A. The results of this comparison are presented in Fig. 9, along with a summary of the values for the peak reverse recovery current ( $I_{rr}$ ) and recovery time ( $t_{rr}$ ) for both the GaN/ $\beta$ -Ga<sub>2</sub>O<sub>3</sub> p-n diode and the 6H-SiC p-n diode in Table 4. Here, the peak reverse recovery current ( $I_{rr}$ ) is defined as the current that occurs during the removal of stored charges in the drift region when the diode switches from the on-state to the off-state. Reverse recovery time ( $t_{rr}$ ) refers to the time it takes for the switching diode to transition from the on-state to the fully off-state.

The results presented in Fig. 9 and Table 4 demonstrate that the GaN/ $\beta$ -Ga<sub>2</sub>O<sub>3</sub> diode has better recovery characteristics than the 6H-SiC diode, with lower  $I_{rr}$  and faster recovery time. The reverse recovery time ( $t_{rr}$ ) is calculated from the moment when the current crosses zero until the reverse recovery current decreases to 10% of  $I_{rr}$ . The presence of electron traps and

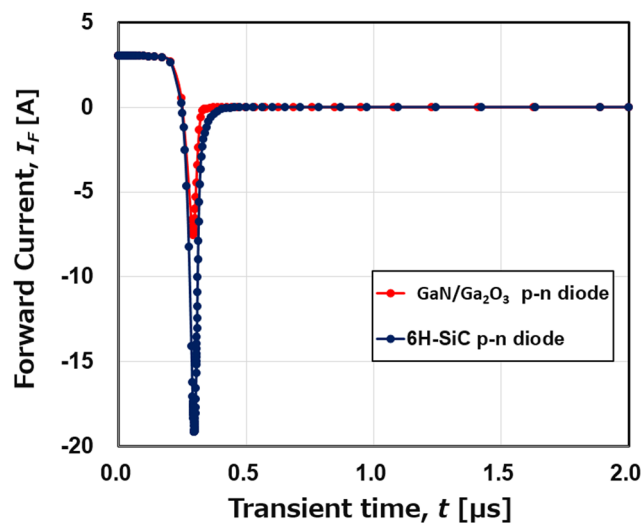


Fig. 9 Simulated reverse recovery characteristics of the GaN/ $\beta$ -Ga<sub>2</sub>O<sub>3</sub> p-n diode compared to the 6H-SiC p-n diode at 300 K.

Table 4 Summary of reverse recovery characteristics

Parameter	GaN/ $\beta$ -Ga <sub>2</sub> O <sub>3</sub> p-n diode	6H-SiC p-n diode
$I_{rr}$ (A)	7.5	19.1
$t_{rr}$ (ns)	72	83



gallium vacancies in Ga<sub>2</sub>O<sub>3</sub> plays a crucial role in enhancing minority carrier recombination, thereby reducing both the reverse recovery time ( $t_{rr}$ ) and the reverse recovery current ( $I_{rr}$ ). In our simulations, defects such as electron and hole traps have been carefully incorporated to reflect their impact on carrier dynamics and diode performance. Previous studies have reported electron traps located near  $E_c - 0.6$  eV,  $E_c - 0.75$  eV, and  $E_c - 1.05$  eV in epitaxial  $\beta$ -Ga<sub>2</sub>O<sub>3</sub> films, as well as the  $E_1$ ,  $E_2$ , and  $E_3$  traps in bulk Ga<sub>2</sub>O<sub>3</sub> crystals.<sup>54–59</sup> Additionally, gallium vacancies, which often form in oxygen-rich environments or during annealing processes, act as electron traps and form high-binding-energy gallium–oxygen vacancy complexes that capture returning holes, further improving the reverse recovery characteristics.<sup>60</sup> Furthermore, we have compared the simulated reverse recovery characteristics of the p-GaN/n-Ga<sub>2</sub>O<sub>3</sub> diode with the experimental results reported for the Si ultrafast diode STTH3012D,<sup>61</sup> as shown in Fig. 10. It is evident that the reverse recovery characteristics of the GaN/ $\beta$ -Ga<sub>2</sub>O<sub>3</sub> diode are superior to those of the Si ultrafast diode STTH3012D. These findings, which are consistent with our defect-inclusive simulations, demonstrate the superior reverse recovery performance of the p-GaN/n-Ga<sub>2</sub>O<sub>3</sub> diode.

Fig. 11 and 12 depict the temperature and forward current dependence of the reverse recovery characteristics of the GaN/ $\beta$ -Ga<sub>2</sub>O<sub>3</sub> p–n diode. In standard diodes, the reverse recovery time and peak reverse recovery current typically increase with temperature due to the accumulation of holes in the n-layer when a forward bias is applied. During the reverse recovery phase, the depletion region extends from the p–n junction into the n-layer. If the width of the depletion region is smaller than the n-layer, the remaining holes in the n-layer recombine and disappear. As the temperature rises, the carrier lifetime increases, causing a delay in recombination and resulting in a longer reverse recovery time. Additionally, as the accumulated holes recombine and the anode voltage recovers, the reverse recovery current continues to rise, leading to an increase in the peak

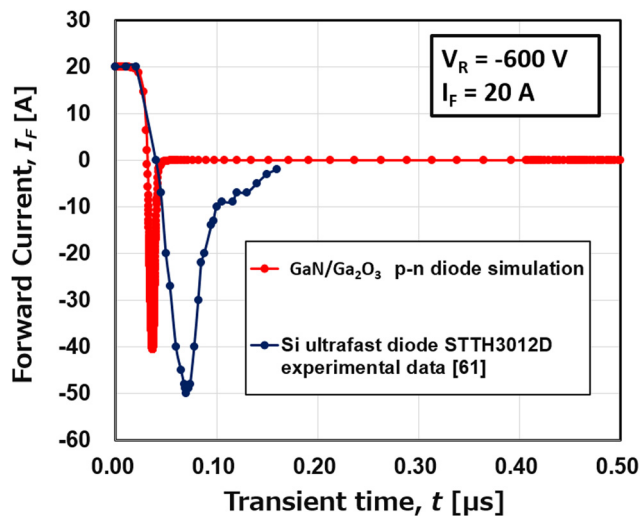


Fig. 10 Comparison of reverse recovery current for the GaN/ $\beta$ -Ga<sub>2</sub>O<sub>3</sub> p–n diode and the Si ultrafast diode STTH3012D.<sup>61</sup>

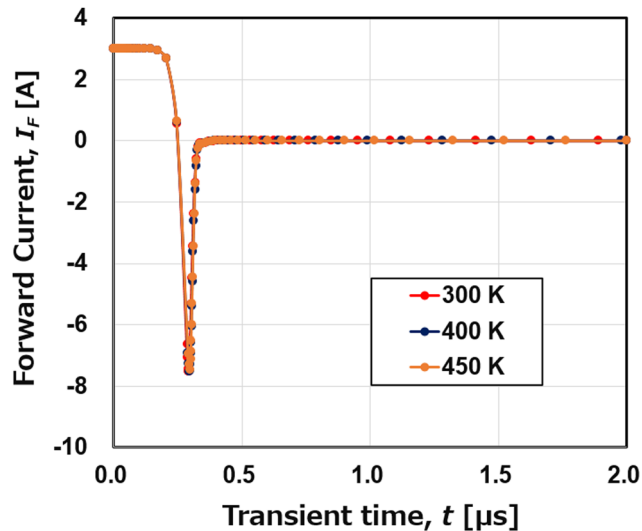


Fig. 11 Simulated temperature-dependent reverse recovery characteristics of the GaN/ $\beta$ -Ga<sub>2</sub>O<sub>3</sub> p–n diode.

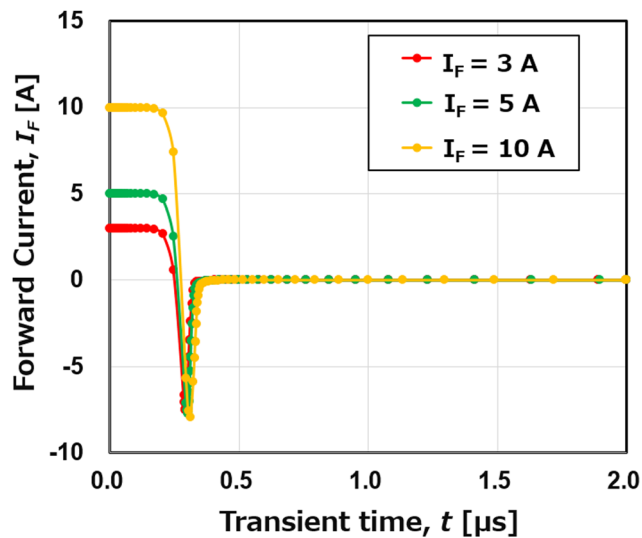


Fig. 12 Simulated forward current-dependent reverse recovery characteristics of the GaN/ $\beta$ -Ga<sub>2</sub>O<sub>3</sub> p–n diode.

reverse recovery current. When the forward current is high, both holes and electrons traverse the junction and enter the opposite region. It takes time for these holes to return, thus the reverse recovery time ( $t_{rr}$ ) becomes longer as the forward current increases.

However, Fig. 11 and 12 demonstrate that the reverse recovery waveforms of the GaN/ $\beta$ -Ga<sub>2</sub>O<sub>3</sub> diode are not affected by changes in temperature or the magnitude of the forward current. Both the peak reverse recovery current ( $I_{rr}$ ) and recovery time ( $t_{rr}$ ) remain nearly constant, regardless of increases in temperature or forward current. This can be attributed to the short carrier lifetimes in both GaN and  $\beta$ -Ga<sub>2</sub>O<sub>3</sub>. The electron lifetime and hole lifetime of n-Ga<sub>2</sub>O<sub>3</sub> are  $2.0 \times 10^{-10}$  s and  $2.1 \times 10^{-8}$  s,<sup>22</sup> respectively, while both the electron and hole lifetimes



of p-GaN are  $1.0 \times 10^{-9}$  s.<sup>40</sup> Additionally, the excellent property of a large critical electric field in GaN and  $\beta$ -Ga<sub>2</sub>O<sub>3</sub> wide-bandgap materials results in a strong electric field in the depletion region, which quickly sweeps out charge carriers and reduces recovery time. Furthermore, the good thermal conductivity of GaN and optimized device design help to minimize the impact of temperature. In contrast, conventional narrow-bandgap semiconductors typically have longer carrier lifetimes and increased reverse recovery time ( $t_{rr}$ ) at higher temperatures. The independence of the diode's reverse recovery characteristics from the forward current ( $I_F$ ) indicates minimal accumulation of minority carriers, which is due to the optimized layer design of the p-GaN/n-Ga<sub>2</sub>O<sub>3</sub> diode structure in this study. The n-Ga<sub>2</sub>O<sub>3</sub> epitaxial layer has a moderate doping concentration of  $4.5 \times 10^{16}$  cm<sup>-3</sup> and a thickness of 3.8  $\mu$ m, while the n-Ga<sub>2</sub>O<sub>3</sub> substrate has a higher doping concentration of  $2.1 \times 10^{18}$  cm<sup>-3</sup> and a thickness of 8.0  $\mu$ m. This design minimizes stored charge during forward conduction, reducing its impact on reverse recovery. In comparison, other structures with lower doping and thicker epitaxial layers were found to store more charge, resulting in increased  $I_{rr}$  and  $t_{rr}$  at higher forward currents. The optimized structure design in our study ensures stable reverse recovery performance, making it suitable for high-speed switching applications. Additionally, F. Zhou *et al.*<sup>62</sup> also reported that the reverse recovery waveform is dominated by capacitive ringing rather than minority carrier recombination in the NiO/Ga<sub>2</sub>O<sub>3</sub> p-n heterojunction diode.

In addition to the effects of temperature and forward current, the doping concentrations of the n-Ga<sub>2</sub>O<sub>3</sub> epitaxial layer and the p-GaN layer significantly influence the reverse recovery characteristics of the GaN/ $\beta$ -Ga<sub>2</sub>O<sub>3</sub> p-n diode. Therefore, our study has been expanded to investigate how variations in doping concentration affect the reverse recovery time ( $t_{rr}$ ) and peak reverse recovery current ( $I_{rr}$ ). We believe that by optimizing the doping levels in the n-Ga<sub>2</sub>O<sub>3</sub> and p-GaN layers, the diode's switching performance and breakdown voltage can be improved. Fig. 13 and 14 demonstrate that the reverse recovery characteristics of the GaN/ $\beta$ -Ga<sub>2</sub>O<sub>3</sub> p-n diode are more affected by changes in the doping concentration of the n-Ga<sub>2</sub>O<sub>3</sub> epitaxial layer than those in the p-GaN layer. As the doping concentration of the n-Ga<sub>2</sub>O<sub>3</sub> epitaxial layer increases, both the peak reverse recovery current ( $I_{rr}$ ) and recovery time ( $t_{rr}$ ) of the GaN/ $\beta$ -Ga<sub>2</sub>O<sub>3</sub> diode also increase. This is because the n-Ga<sub>2</sub>O<sub>3</sub> layer acts as the drift region, storing charge carriers during forward conduction. A higher doping concentration results in a larger amount of stored charge, leading to a higher reverse recovery current and a longer recovery time. This effect is further amplified by the relatively short electron lifetime ( $2.0 \times 10^{-10}$  s) and longer hole lifetime ( $2.1 \times 10^{-8}$  s) in the n-Ga<sub>2</sub>O<sub>3</sub> layer. The short electron lifetime allows for rapid electron removal, while the longer hole lifetime delays recombination, thereby extending the reverse recovery time. In contrast, the electron and hole lifetimes of approximately 1.0 ns in the p-GaN layer<sup>40</sup> primarily affect the forward conduction process rather than the reverse recovery. Therefore, changes in the doping concentration of the n-Ga<sub>2</sub>O<sub>3</sub> layer have a greater

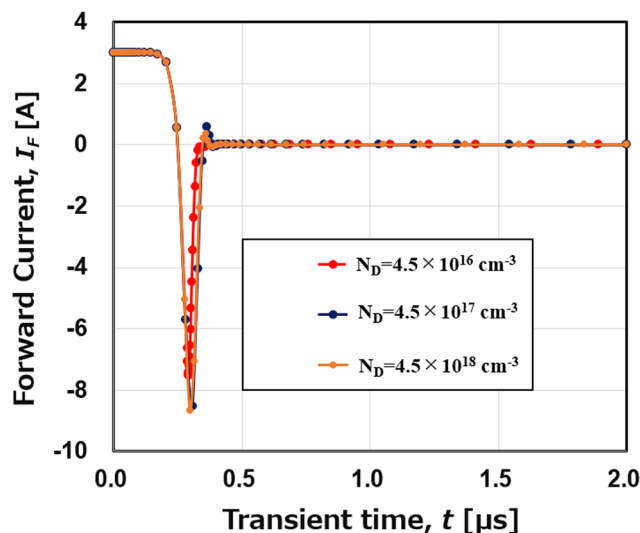


Fig. 13 Simulated n-Ga<sub>2</sub>O<sub>3</sub> epitaxial layer doping concentration-dependent reverse recovery characteristics of the GaN/ $\beta$ -Ga<sub>2</sub>O<sub>3</sub> p-n diode.

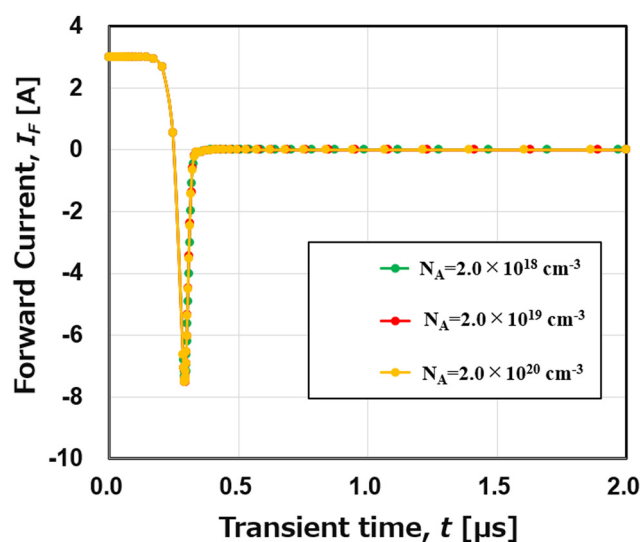


Fig. 14 Simulated p-GaN layer doping concentration-dependent reverse recovery characteristics of the GaN/ $\beta$ -Ga<sub>2</sub>O<sub>3</sub> p-n diode.

impact on the reverse recovery characteristics of the GaN/ $\beta$ -Ga<sub>2</sub>O<sub>3</sub> p-n diode than those in the p-GaN layer.

## 4. Conclusion

Our simulations of the GaN/ $\beta$ -Ga<sub>2</sub>O<sub>3</sub> p-n heterojunction diode showed a turn-on voltage of 3.5 V and a breakdown voltage of 703 V at 300 K, with stable performance across different temperatures. This stability highlights the potential application of the p-GaN/n-Ga<sub>2</sub>O<sub>3</sub> heterojunction diode as a reliable power device for high-voltage operations. In the reverse recovery simulation, the GaN/ $\beta$ -Ga<sub>2</sub>O<sub>3</sub> diode demonstrated fast





- Breakdown Voltage of Over 750 V, *IEEE Electron Device Lett.*, 2016, **37**(2), 212–215.
- 17 A. J. Green, K. D. Chabak, E. R. Heller, R. C. Fitch, M. Baldini, A. Fiedler, K. Irmscher, G. Wagner, Z. Galazka, S. E. Teltak, A. Crespo, K. Leedy and G. H. Jessen, 3.8-MV cm<sup>-1</sup> Breakdown Strength of MOVPE-Grown Sn-Doped  $\beta$ -Ga<sub>2</sub>O<sub>3</sub> MOSFETs, *IEEE Electron Device Lett.*, 2016, **37**(7), 902–905.
  - 18 S. Krishnamoorthy, Z. Xia, S. Bajaj, M. Brenner and S. Rajan, Delta-doped  $\beta$ -gallium oxide field-effect transistor, *Appl. Phys. Express*, 2017, **10**, 051102.
  - 19 E. Ahmadi, O. S. Koksaldi, X. Zheng, T. Mates, Y. Oshima, U. K. Mishra and J. S. Speck, Demonstration of  $\beta$ -(Al<sub>x</sub>Ga<sub>1-x</sub>)<sub>2</sub>O<sub>3</sub>/ $\beta$ -Ga<sub>2</sub>O<sub>3</sub> modulation doped field-effect transistors with Ge as dopant grown via plasma-assisted molecular beam epitaxy, *Appl. Phys. Express*, 2017, **10**, 071101.
  - 20 N. Moser, J. McCandless, A. Crespo, K. Leedy, A. Green, A. Neal, S. Mou, E. Ahmadi, J. Speck, K. Chabak, N. Peixoto and G. Jessen, Ge-Doped  $\beta$ -Ga<sub>2</sub>O<sub>3</sub> MOSFETs, *IEEE Electron Device Lett.*, 2017, **38**(6), 775–778.
  - 21 M. Higashiwaki, K. Sasaki, A. Kuramata, T. Masui and S. Yamakoshi, Gallium oxide (Ga<sub>2</sub>O<sub>3</sub>) metal–semiconductor field-effect transistors on single-crystal  $\beta$ -Ga<sub>2</sub>O<sub>3</sub> (010) substrates, *Appl. Phys. Lett.*, 2012, **100**, 013504.
  - 22 K. Wang, Z. Wang, R. Cao, H. Liu, W. Chang, L. Zhao, B. Mei, H. Lv, X. Zeng and Y. Xue, Study of the mechanism of single event burnout in lateral depletion-mode Ga<sub>2</sub>O<sub>3</sub> MOSFET devices via TCAD simulation, *J. Appl. Phys.*, 2024, **135**, 145702.
  - 23 H. H. Gong, X. H. Chen, Y. Xu, F.-F. Ren, S. L. Gu and J. D. Ye, A 1.86-kV double-layered NiO/ $\beta$ -Ga<sub>2</sub>O<sub>3</sub> vertical p–n heterojunction diode, *Appl. Phys. Lett.*, 2020, **117**, 022104.
  - 24 W. Hao, Q. He, K. Zhou, G. Xu, W. Xiong, X. Zhou, G. Jian, C. Chen, X. Zhao and S. Long, Low defect density and small *I*–*V* curve hysteresis in NiO/ $\beta$ -Ga<sub>2</sub>O<sub>3</sub> pn diode with a high PFOM of 0.65 GW cm<sup>-2</sup>, *Appl. Phys. Lett.*, 2021, **118**, 043501.
  - 25 T. Watahiki, Y. Yuda, A. Furukawa, M. Yamamura, Y. Takiguchi and A. Miyajima, Heterojunction p-Cu<sub>2</sub>O/n-Ga<sub>2</sub>O<sub>3</sub> diode with high breakdown voltage, *Appl. Phys. Lett.*, 2017, **111**, 222104.
  - 26 H. Gong, F. Zhou, W. Xu, X. Yu, Y. Xu, Y. Yang, F. Ren, S. Gu, Y. Zheng, R. Zhang, H. Lu and J. Ye, 1.37 kV/12 A NiO/ $\beta$ -Ga<sub>2</sub>O<sub>3</sub> Heterojunction Diode With Nanosecond Reverse Recovery and Rugged Surge-Current Capability, *IEEE Trans. Power Electron.*, 2021, **36**(11), 12213–12217.
  - 27 X. Lu, X. Zhou, H. Jiang, Z. Chen, Y. Pei, K. M. Lau and G. Wang, 1-kV Sputtered p-NiO/n-Ga<sub>2</sub>O<sub>3</sub> Heterojunction Diodes with an Ultra-Low Leakage Current Below 1  $\mu$ A cm<sup>-2</sup>, *IEEE Electron Device Lett.*, 2020, **41**(3), 449–452.
  - 28 J. Montes, C. Yang, H. Fu, T.-H. Yang, K. Fu, H. Chen, J. Zhou, X. Huang and Y. Zhao, Demonstration of mechanically exfoliated  $\beta$ -Ga<sub>2</sub>O<sub>3</sub>/GaN p–n heterojunction, *Appl. Phys. Lett.*, 2019, **114**(16), 162103.
  - 29 D. H. Mudiyaşelage, D. Wang and H. Fu, Wide Bandgap Vertical kV-class  $\beta$ -Ga<sub>2</sub>O<sub>3</sub>/GaN Heterojunction p–n Power Diodes with Mesa Edge Termination, *IEEE J. Electron Devices Soc.*, 2022, **10**, 89–97.
  - 30 E. Hossain, A. A. Rahman, M. Gokhale, R. Kulkarni, R. Mondal, A. Thamizhavel and A. Bhattacharya, Growth of high-quality GaN on (1 0 0) Ga<sub>2</sub>O<sub>3</sub> substrates by facet-controlled MOVPE, *J. Cryst. Growth*, 2019, **524**, 125165.
  - 31 S. Leone, R. Fornari, M. Bosi, V. Montedoro, L. Kirste, P. Doering, F. Benkhelifa, M. Prescher, C. Manz, V. Polyakov and O. Ambacher, Epitaxial growth of GaN/Ga<sub>2</sub>O<sub>3</sub> and Ga<sub>2</sub>O<sub>3</sub>/GaN heterostructures for novel high electron mobility transistors, *J. Cryst. Growth*, 2020, **534**, 125511.
  - 32 W. Li, X. Zhang, J. Zhao, J. Yan, Z. Liu, J. Wang, J. Li and T. Wei, Rectification behavior of polarization effect induced type-II n-GaN/n-type  $\beta$ -Ga<sub>2</sub>O<sub>3</sub> isotype heterojunction grown by metal organic vapor phase epitaxy, *J. Appl. Phys.*, 2020, **127**(1), 015302.
  - 33 K. Irmscher, Z. Galazka, M. Pietsch, R. Uecker and R. Fornari, Electrical properties of  $\beta$ -Ga<sub>2</sub>O<sub>3</sub> single crystals grown by the Czochralski method, *J. Appl. Phys.*, 2011, **110**(6), 063720.
  - 34 K. Ghosh and U. Singiseti, Impact ionization in  $\beta$ -Ga<sub>2</sub>O<sub>3</sub>, *J. Appl. Phys.*, 2018, **124**(8), 085707.
  - 35 I. Vurgaftman, J. R. Meyer and L. R. Ram-Mohan, Band parameters for III–V compound semiconductors and their alloys, *J. Appl. Phys.*, 2001, **89**(11), 5815–5875.
  - 36 O. Madelung, U. Rössler and M. Schulz, *Group IV Elements, IV–IV and III–V Compounds. Part b – Electronic, Transport, Optical and Other Properties*, Springer-Verlag, Berlin Heidelberg, 2002.
  - 37 S. N. Mohammad and H. Morkoç, Progress and prospects of group-III nitride semiconductors, *Prog. Quantum Electron.*, 1996, **20**(5–6), 361–525.
  - 38 G. Sabui, P. J. Parbrook, M. Arredondo-Arechavala and Z. J. Shen, Modeling and simulation of bulk gallium nitride power semiconductor devices, *AIP Adv.*, 2016, **6**(5), 055006.
  - 39 B. J. Baliga, Gallium nitride devices for power electronic applications, *Semicond. Sci. Technol.*, 2013, **28**, 074011.
  - 40 G. F. Brown, J. W. Ager, W. Walukiewicz and J. Wu, Finite element simulations of compositionally graded InGaN solar cells, *Sol. Energy Mater. Sol. Cells*, 2010, **94**, 478–483.
  - 41 X. A. Cao, H. Lu, S. F. LeBoeuf, C. Cowen, S. D. Arthur and W. Wang, Growth and characterization of GaN PiN rectifiers on free-standing GaN, *Appl. Phys. Lett.*, 2005, **114**(87), 053503.
  - 42 C. Liu, E. F. Chor and L. S. Tan, Enhanced device performance of AlGaN/GaN HEMTs using HfO<sub>2</sub> high-*k* dielectric for surface passivation and gate oxide, *Semicond. Sci. Technol.*, 2007, **22**, 522–527.
  - 43 M. Ruff, H. Mitlenher and R. Helbig, SiC devices: physics and numerical simulation, *IEEE Trans. Electron Devices*, 1994, **41**, 1040–1054.
  - 44 P. T. Landsberg and G. S. Kousik, The connection between carrier lifetime and doping density in nondegenerate semiconductors, *J. Appl. Phys.*, 1984, **56**, 1696–1700.
  - 45 A. Galeckas, J. Linnros, V. Grivickas, U. Lindefelf and C. Hallin, Auger recombination in 4H-SiC: unusual temperature behaviour, *Appl. Phys. Lett.*, 1997, **71**, 3269–3271.
  - 46 P. Losee, *Design, fabrication and characterization of high voltage 4H-SiC junction rectifiers for power switching*



- application*, PhD dissertation, Rensselaer Polytechnic Institute, New York, 2007.
- 47 Q. Song, T. Xiaoyan, H. Yuan, C. Han and Y. Zhang, Design, Simulation and Fabrication of 4H-SiC power SBDs with SIPOS FP structure, *IEEE Trans. Device Mater. Reliab.*, 2015, **15**, 543–551.
  - 48 S. M. Sze, *Physics of Semiconductor devices*, Wiley, New York, NY, USA, 1981.
  - 49 R. Raghunathan and B. J. Baliga, Temperature dependence of hole impact ionization coefficients in 4H and 6H-SiC, *Solid-State Electron.*, 1999, **43**(2), 199–211.
  - 50 M. H. Wong, Y. Morikawa, K. Sasaki, A. Kuramata, S. Yamakoshi and M. Higashiwaki, Characterization of channel temperature in Ga<sub>2</sub>O<sub>3</sub> metal-oxide-semiconductor field-effect transistors by electrical measurements and thermal modeling, *Appl. Phys. Lett.*, 2016, **109**, 193503.
  - 51 Y. Duan, J. Wang, Z. Zhu, G. Piao, K. Ikenaga, H. Tokunaga, S. Koseki, M. Bulsara and P. Fay, Ion-implanted triple-zone graded junction termination extension for vertical GaN p–n diodes, *Appl. Phys. Lett.*, 2023, **122**, 212104.
  - 52 K. Fujihira, S. Tamura, T. Kimoto and H. Matsunami, Low-Loss, High-Voltage 6H-SiC Epitaxial p–i–n Diode, *IEEE Trans. Electron Devices*, 2002, **49**(1), 150–154.
  - 53 L. Latu-Romain and M. Ollivier, *Silicon Carbide One-dimensional Nanostructures*, edn 2015, WILEY-ISTE London, United Kingdom, 2015, pp. 1–148.
  - 54 A. Y. Polyakov, N. B. Smirnov, I. V. Shchemerov, E. B. Yakimov, J. Yang, F. Ren, G. Yang, J. Kim, A. Kuramata and S. J. Pearton, Point defect induced degradation of electrical properties of Ga<sub>2</sub>O<sub>3</sub> by 10 MeV proton damage, *Appl. Phys. Lett.*, 2018, **112**, 032107.
  - 55 Z. Zhang, E. Farzana, A. R. Arehart and S. A. Ringel, Deep level defects throughout the bandgap of (010) β-Ga<sub>2</sub>O<sub>3</sub> detected by optically and thermally stimulated defect spectroscopy, *Appl. Phys. Lett.*, 2016, **108**, 052105.
  - 56 Y. Nakano, Electrical Characterization of β-Ga<sub>2</sub>O<sub>3</sub> Single Crystal Substrates, *ECS J. Solid State Sci. Technol.*, 2017, **6**, 615.
  - 57 M. E. Ingebrigtsen, J. B. Varley, A. Y. Kuznetsov, B. G. Svensson, G. Alfieri, A. Mihaila, U. Badstübner and L. Vines, Iron and intrinsic deep level states in Ga<sub>2</sub>O<sub>3</sub>, *Appl. Phys. Lett.*, 2018, **112**, 042104.
  - 58 M. Labed, N. Sengouga, C. V. Prasad, M. Henini and Y. S. Rim, On the nature of majority and minority traps in β-Ga<sub>2</sub>O<sub>3</sub>: a review, *Mater. Today Phys.*, 2023, **36**, 101155.
  - 59 E. Farzana, E. Ahmadi, J. S. Speck, A. R. Arehart and S. A. Ringel, Deep level defects in Ge-doped (010) β-Ga<sub>2</sub>O<sub>3</sub> layers grown by plasma-assisted molecular beam epitaxy, *J. Appl. Phys.*, 2018, **123**, 161410.
  - 60 K. Zeng, Z. Bian, N. Sinha and S. Chowdhury, Simultaneous drive-in of Mg and disassociation of Mg–H complex in Ga<sub>2</sub>O<sub>3</sub> by oxygen annealing achieving remarkable current blocking, *Appl. Phys. Lett.*, 2024, **124**, 212102.
  - 61 S. Yin, Y. Liu, Y. Liu, K. J. Tseng, J. Pou and R. Simanjorang, Comparison of SiC Voltage Source Inverters Using Synchronous Rectification and Freewheeling Diode, *IEEE Trans. Ind. Electron.*, 2018, **65**(2), 1051–1061.
  - 62 F. Zhou, H. Gong, M. Xiao, Y. Ma, Z. Wang, X. Yu, L. Li, L. Fu, H. H. Tan, Y. Yang, F.-F. Ren, S. Gu, Y. Zheng, H. Lu, R. Zhang, Y. Zhang and J. Ye, An avalanche-and-surge robust ultrawidebandgap heterojunction for power electronics, *Nat. Commun.*, 2023, **14**, 4459.

